

Vortex states in mesoscopic three-band superconductors

San Gillis,¹ Juha Jäykkä,² and Milorad V. Milošević¹

¹*Departement Fysica, Universiteit Antwerpen, Groenenborgerlaan 171, B-2020 Antwerpen, Belgium*

²*Nordita, KTH Royal Institute of Technology and Stockholm University Roslagstullsbacken 23, SE-106 91 Stockholm, Sweden*

(Dated: October 15, 2021)

Using multi-component Ginzburg-Landau simulations, we show a plethora of vortex states possible in mesoscopic three-band superconductors. We find that mesoscopic confinement stabilizes chiral states, with non-trivial phase differences between the band-condensates, as the ground state of the system. As a consequence, we report the broken-symmetry vortex states, the chiral states where vortex cores in different band condensates do not coincide (split-core vortices), as well as fractional vortex states with broken time-reversal symmetry.

I. INTRODUCTION

MgB₂ was discovered to be superconducting in 2001¹, as a first two-gap superconductor, with the highest critical temperature $T_c = 39K$ of all binary compound metallic superconductors known today. Comparing with other known electron-phonon mediated superconductors, this T_c is exceptionally high, and is thought to be due to the interaction between the two superconducting gaps. These gaps have been experimentally measured using scanning tunneling spectroscopy^{2,3}, point contact spectroscopy^{4,5} and heat capacity experiments^{6,7}. Although multiband superconductors have been theoretically proposed over fifty years ago^{8,9}, it was only after this discovery that there was renewed theoretical and experimental interest in multiband superconductivity.

Two-band superconductors can exhibit new phenomena not present in conventional single band superconductors. It was theoretically predicted that there could exist vortex states with non monotonic inter-vortex interactions, namely short range repulsion and long range attraction due to competing length scales of the two bands¹⁰⁻¹⁴, resulting in unusual vortex patterns^{15,16}. Not only is the interaction between vortices markedly different from the single band case, but it is also possible to stabilize fractional vortices in multiband superconductors¹⁷⁻¹⁹. Another new phenomenon that occurs in two-band superconductors is that of hidden criticality²⁰. When two gaps are weakly coupled, the coherence length of the weaker band shows a pronounced peak close to a hidden critical temperature, in stark contrast with the monotonic behavior of the coherence length as a function of temperature in single band superconductors.

Related to length-scales, it is well known that confined superconductivity on the mesoscopic scale brings forth interesting behavior, such as enhancement of critical magnetic field^{21,22} or the Little-Parks effect^{23,24}. Additionally, the boundary can impose its symmetry on the vortex matter, enabling e.g. formation of giant vortices^{21,25-29}. For two gap superconductors it was shown that non composite and fractional vortex states can be thermodynamically stabilized by the mesoscopic boundary³⁰⁻³⁶, due to different interaction of two band-

condensates with the mesoscopic confinement.

The recent discovery of iron-based superconductors³⁷⁻³⁹ has further increased interest in multiband superconductors, since these materials typically have more than two coupled superconducting bands^{40,41}. The coupling can impose a phase difference between the different components of the superconducting order parameter. This allows inherently new physics not present in single band or two band superconductors, due to frustration between the phase locking tendencies, leading to states with spontaneously broken time reversal symmetry (BTRS)⁴²⁻⁴⁵. These states allow magnetic flux-carrying topological solitons, with distinct magnetic signatures, which should be observable in experiments.

In Refs.^{42,43} the topological solitons with broken time reversal symmetry were considered in bulk superconducting samples. In this paper, we study the influence of the mesoscopic confinement on the BTRS states. We look at a system with one strong superconducting band, which couples to two other bands which are only superconducting due to the interaction with the first band (the usual situation for temperatures close to T_c). The coupling between bands is of the form $(++-)$, meaning that the order parameters of second and third band prefer to have a phase difference of π while trying to attain the same phase as the first band. It is clear that this can lead to frustration, and non-trivial phase differences between the bands. As we will show, such chiral superconducting state is indeed stable, and becomes the ground state in mesoscopic samples. Moreover, the mesoscopic boundary interacts with the phase domain walls in the sample. Those domain walls energetically favor splitting of vortex lines in different bands, and their interaction with mesoscopic boundary enables a plethora of possible states unattainable in bulk or non-chiral mesoscopic samples - including chiral fractional vortices, where vorticity is not equal in all band condensates in addition to broken time-reversal symmetry. We finally offer a classification of the observed vortex states, richer than ones found in any other superconducting system studied to date.

The paper is organized as follows. In Sec. II we introduce the Ginzburg-Landau model for three-component superconductors. We express the Ginzburg-Landau coefficients in the microscopic framework to facilitate com-

parison with experiment. In Sec. III we discuss the observed vortex states and order them in three main classes, with several subdivisions. Our summary and conclusions are given in Sec. IV.

II. THEORETICAL FORMALISM

In this paper, we perform theoretical simulations in the framework of the three-component Ginzburg-Landau model. The governing energy functional takes the form:

$$\begin{aligned} \mathcal{F} = \int dV \left[\sum_{i=1}^3 \left(\alpha_i |\Psi_i|^2 + \frac{1}{2} \beta_i |\Psi_i|^4 \right) \right. \\ \left. - \sum_{i=0}^3 \sum_{j>i}^3 \eta_{ij} |\Psi_i| |\Psi_j| \cos(\phi_i - \phi_j) \right. \\ \left. + \sum_{i=1}^3 \frac{1}{2m_i} \left| \left(-i\hbar\nabla - \frac{2e}{c} \vec{A} \right) \Psi_i \right|^2 + \frac{(\nabla \times \vec{A})^2}{8\pi} \right], \quad (1) \end{aligned}$$

where \mathcal{F} is the difference in free energy between the superconducting and normal state, Ψ_i are the complex order parameters of the band-condensates (with phase ϕ_i), \vec{A} is the vector potential, α_i , β_i are the phenomenological GL coefficients, η_{ij} denote the ‘Josephson’ couplings between the bands, and i and j are the band indices.

We next rewrite Eq. (1) in a dimensionless form, by scaling length to units of $\xi_1 = \hbar/\sqrt{-2m_1\alpha_1}$, the order parameters to $\Psi_{10} = -\alpha_1/\beta_1$, the vector potential to $A_0 = \hbar c/2e\xi_1$ (thus magnetic field is scaled to $H_{c_2}^{(1)} = \hbar c/2e\xi_1^2$) and free energy to $\mathcal{F}_0 = \xi_1^3\alpha_1^2V/\beta_1$, where V is the volume of the sample. The dimensionless energy functional reads:

$$\begin{aligned} \frac{\mathcal{F}}{\mathcal{F}_0} = \frac{1}{V} \int dV \left[\sum_{i=1}^3 \left(\frac{\alpha_i}{|\alpha_1|} |\Psi_i|^2 + \frac{1}{2} \frac{\beta_i}{\beta_1} |\Psi_i|^4 \right) \right. \\ \left. - \sum_{i=0}^3 \sum_{j>i}^3 \frac{\eta_{ij}}{|\alpha_1|} |\Psi_i| |\Psi_j| \cos(\phi_i - \phi_j) \right. \\ \left. + \sum_{i=1}^3 \frac{m_1}{m_i} \left| \left(\nabla - i\vec{A} \right) \Psi_i \right|^2 + \kappa_1^2 (\nabla \times \vec{A})^2 \right], \quad (2) \end{aligned}$$

where $\kappa_1 = (H_{c_2}^{(1)})^2 \xi_1^3 / 8\pi \mathcal{F}_0 V$. The free energy is then minimized numerically in order to obtain solutions to the GL model. The fields found from this minimization will

automatically be solutions to the equations of motion:

$$\begin{aligned} \frac{\alpha_i}{|\alpha_1|} \psi_i + \frac{\beta_i}{\beta_1} |\psi_i|^2 \psi_i \\ - \sum_{j \neq i} \frac{\eta_{ij}}{|\alpha_1|} \psi_j + \frac{m_1}{m_i} (\nabla - i\vec{A})^2 \psi_i = 0, \quad (3) \end{aligned}$$

$$\begin{aligned} \vec{J} = \sum_{i=1}^3 \vec{J}_i = \nabla \times \nabla \times \vec{A} \\ = \sum_{i=1}^3 \frac{m_1}{2m_i \kappa_1^2} \left(i (\bar{\psi}_i \nabla \psi_i - \psi_i \nabla \bar{\psi}_i) + |\psi_i|^2 \vec{A} \right). \quad (4) \end{aligned}$$

To closer relate our results to known superconducting materials, we express the GL coefficients in terms of microscopic parameters, following Ref.⁴⁵, as

$$\alpha_i = N(0) \gamma_{ii} - N_i(0) \mathcal{A} - N_i(0) \tau, \quad (5)$$

$$\beta_i = N_i(0) \frac{7\zeta(3)}{8\pi^2 T_c}, \quad (6)$$

$$\kappa_i = \frac{\hbar^2}{2m_i} = \xi_i^2 |\alpha_i| = \frac{\beta_i}{6} \hbar^2 v_i^2, \quad (7)$$

$$\eta_{ij} = N(0) \gamma_{ij}, \quad (8)$$

where $N(0) = \sum_{i=1}^3 N_i(0)$ is the total density of states, $\mathcal{A} = \ln((2e^\Gamma \hbar \omega_D) / (\pi T_c))$ with Γ the Euler constant and ω_D the Debye energy, and $\tau = \ln(T/T_c)$. v_i are the band dependent Fermi velocities, and γ_{ij} denote the elements of the inverted interaction matrix.

Considering that microscopic parameters of relevant materials are not yet known with certainty, in what follows we will choose a set of Ginzburg-Landau parameters, and just note that it is possible to integrate real microscopic parameters in the study:

$$\begin{aligned} \frac{\alpha_i}{|\alpha_1|} &= \left(-1, \frac{2}{3}, \frac{2}{3} \right), \\ \frac{\beta_i}{\beta_1} &= (1, 1, 1), \\ \frac{\eta_{ij}}{|\alpha_1|} &= \left(\frac{2}{3}, \frac{2}{3}, -2 \right), \\ \frac{m_1}{m_i} &= (1, 1, 1). \end{aligned}$$

With this choice of parameters, we consider three bands with same parameters except for the elements in the interaction matrix, i.e. only the coupling constants between the bands will differ, as well as the respective critical temperatures of the bands. Such choice will enable us to more easily differentiate the effects of chirality from the other forms of competition between the band condensates.

In the numerical approach, we search for as many solutions as possible to the equations of motion Eq. (3) and (4). We do this by starting from four different initial configurations: (i) the Meissner state with no phase difference between the condensates, (ii) the Meissner state

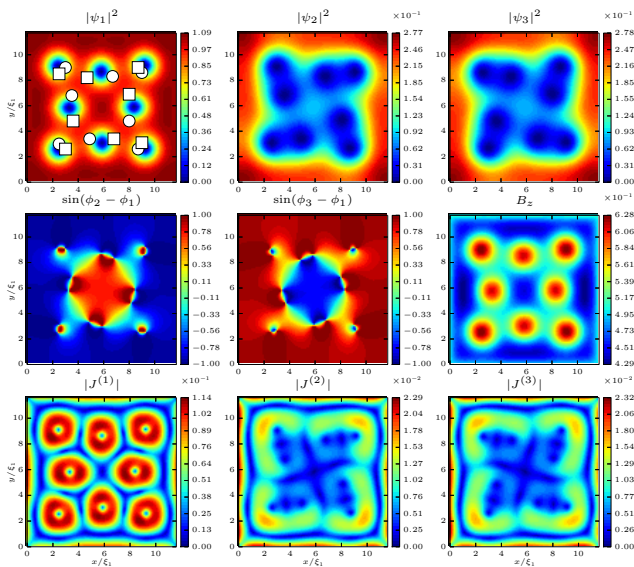


FIG. 1: One of the four initial states used in the simulations, created by shrinking the known ($N = 8$, see Ref.⁴²) soliton solution for bulk three-band superconductors to a mesoscopic size. Different panels show: the Cooper-pair density of different band-condensates ($\psi_{i=1,2,3}$), the phase difference between the bands, spatial distribution of the total magnetic field B_z , and magnitude of the three components to the current ($J_{i=1,2,3}$), each stemming from a different band-condensate. In the Cooper-pair density plot for the first condensate (top-left panel), the locations of vortices in the second and the third condensate are shown by white dots and squares respectively.

with phase difference between the condensates, (iii) a field-cooled condition, i.e. weak and fluctuating order parameter in each band, and (iv) a state found by recreating the $N = 8$ soliton solution from Ref.⁴² and shrinking this state to a size of $12\xi_1$ by $12\xi_1$. The exemplary result of latter operation is shown in Fig. 1. From each of the initial states, we sweep the external magnetic field up and down. At certain values of the magnetic field, the system will jump to a new state with different vorticity. These states are saved, and from each new state, we do a new sweep of the magnetic field in both directions to uncover other possible states.

A. Numerical scheme

At every value of the magnetic field in a sweep, we re-relax the free energy in order to find a solution to the equations of motion at that magnetic field. We do this by using the standard link-variable discretisation scheme with one-point forward differences to discretise the energy functional \mathcal{F} on a square lattice of spacing h . The lattice is subdivided in $N_i \times N_j$ points, and $N_i = N_j = 120$ in all simulations reported in this paper. This discretisation has been used before in Ref.¹⁹, however it is now extended to include an arbitrary number of complex order parameters and the corresponding

Josephson couplings. The applied magnetic field \mathbf{B} is implemented by giving \mathbf{A} a boundary condition such that $\nabla \times \mathbf{A} = \mathbf{B}$ on the boundary.

Given an initial configuration (ψ_i, \mathbf{A}) we used either the quasi-Newton BFGS or conjugate gradient method, as implemented by the TAO⁴⁶ and PETSc⁴⁷ parallel numerical libraries, to find a local minimum of \mathcal{F} . Other parts of the program and support routines are an adaptation of previous work done in Ref.⁴⁸. More details on the discretisation can be found in Refs.^{49,50}.

III. CLASSIFICATION OF VORTEX STATES

In this section we will classify in a comprehensive manner the many states found using the recipe described in the previous section. It is well known that even in single-band superconductors at a given external magnetic field there are multiple states possible, one ground state, and other meta-stable states - but all realizable in experiment. This can be accomplished for example by increasing the magnetic field until a new state with different vorticity emerges. If the magnetic field is subsequently decreased again, the new vortex state will not be destroyed immediately, thus one has found two different vortex states at a given magnetic field. As it turns out, the number of meta-stable states in three-band superconductors is far larger than in any single-band counterpart. Using the characteristic features of those states, we classify them in three main categories.

A. Conventional vortex states

Vortex matter in mesoscopic single band superconductors is well understood (see Refs.^{21,29} and citing articles) and we will refer to similar states in three band superconductors as ‘conventional vortex states’. They comprise composite vortices, vortex configurations influenced by the geometry of the sample, and no phase difference between the band-condensates.

Fig. 2 shows the energy dependence of all the conventional vortex states found during the simulations as a function of the externally applied magnetic field. Due to the Josephson coupling between the condensates, the second and third condensate become superconducting. Since there is no phase difference between the condensates, the passive bands have the same behavior as the active band.

We note that states for each vorticity have one corresponding curve, except for vorticity four, which has two. In Fig. 3(a) we show the lowest energy $L = 4$ state, while Fig. 3(b) shows the another stable state but with higher energy. State in Fig. 3(b) is usually not found stable in single-band superconductors, which demonstrates subtly different interplay of (multi-cored) vortices with screening Meissner currents at the boundary of the multiband

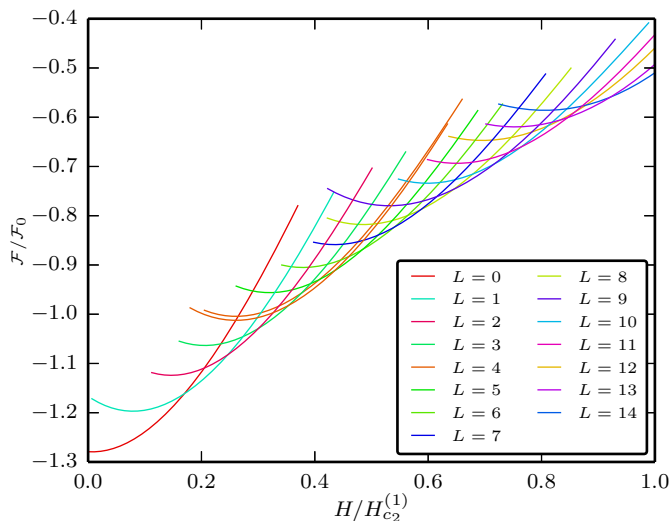


FIG. 2: Energy of all found conventional (composite, not fractional, not chiral) vortex states as a function of the applied external magnetic field. L denotes the vorticity of the state.

samples. In what follows, we show that differences are actually very pronounced.

B. Chiral vortex states

It has already been shown in Refs.^{42,44,45} that it is possible for three-band superconductors to have solutions with a phase difference between band-condensates, which we refer to as chiral solutions. Fig. 4 shows the energy of all found chiral vortex states, with same vorticity in all bands. It is clear that the basic shape of Fig. 4 is the same as in Fig. 2, but more importantly - the chiral states always have lower energy than the corresponding conventional state! Since for the same parameters Ref.⁴² reported chiral states as higher energy ones, it is implied from our results that mesoscopic confinement enhances the chiral states and lowers their energy compared to the conventional states. Another important feature of chiral states is that they exhibit much larger meta-stability, i.e. more possibilities for a given vorticity. For example, we show in Fig. 5 the chiral counterparts of + and \times configurations from Fig. 3. However, we also find different configurations for vorticity six for example, as shown in Fig. 6. These are not present among the conventional vortex states.

Another factor introducing excitations into the spectrum of chiral states with given vorticity are phase domain walls. These domain walls were identified as a source of split-core vortex states in bulk three-component samples in Ref.⁴², i.e. states in which vortex cores do not coincide in different band-condensates. In Fig. 7 we show the split-core $L = 4$ state (c.f. Fig. 5) where vortices in different bands minimize energy by separating along the internal phase domain wall (connecting the vortices,

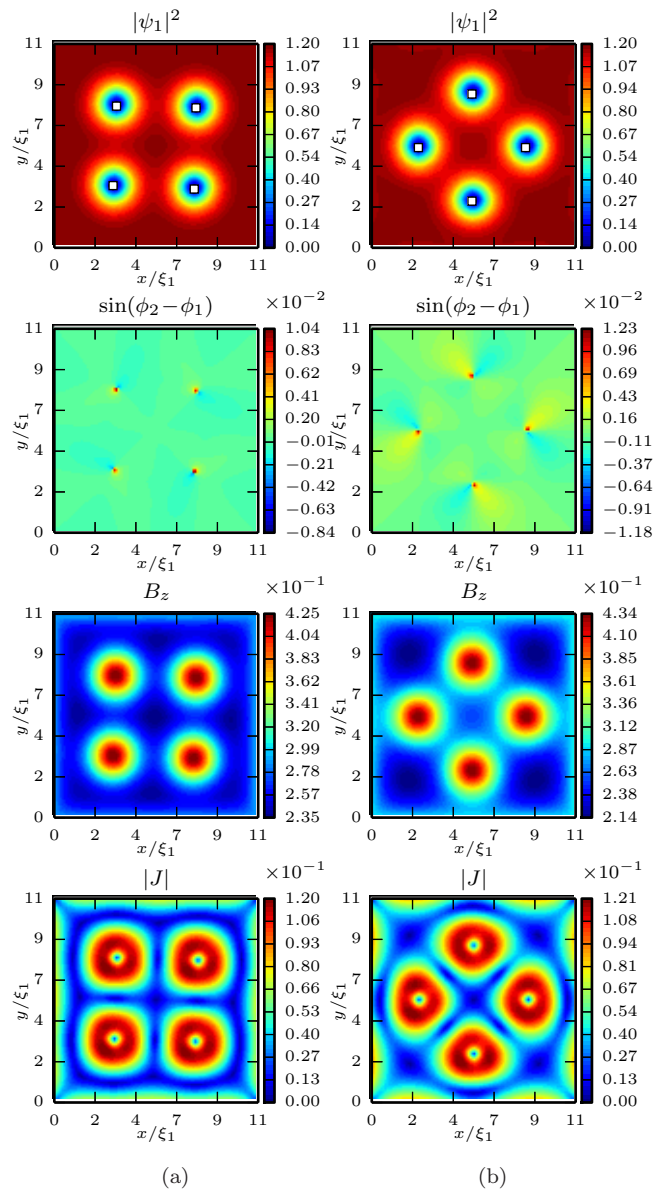


FIG. 3: Conventional vortex state with vorticity $L = 4$ in all bands (a), and an alternative higher energy state (b). Panels (top to bottom) show the Cooper-pair density of the first band with superimposed locations of vortices in other bands, the phase difference between the band condensates 1 and 2, the distribution of the magnetic field, and total current in the sample.

see the plot of phase difference in Fig. 7). However, this split-core vortex state has higher energy than both states of Fig. 5. Fig. 8 shows the energy of all found chiral states with domain walls, i.e. with split-core vortices. We note three longer curves of vorticity four, six and eight. These are states with internal domain walls as in Fig. 7. These states are more stable than the other states in Fig. 8, and are not present for every vorticity - due to the competition of the vortex configuration

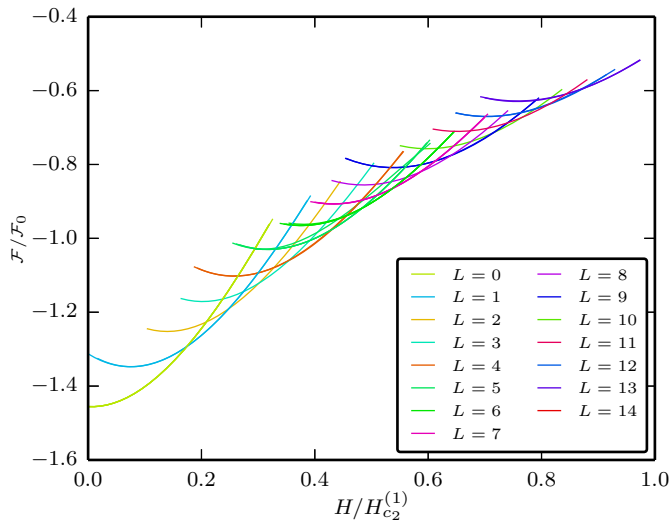


FIG. 4: Energy of all found chiral composite vortex states as a function of the applied external magnetic field.

with the sample geometry (i.e. its C_4 symmetry). These states are typically found in the simulations from the initial state shown in Fig. 1. States with different vorticity and an internal domain wall were not found.

However, besides the states with an internal domain wall, we found other states where the domain walls connect with the sample boundary - which is a new mesoscopic effect. These states are very rich, and can form from an arbitrary initial condition - e.g. corresponding to a field-cooled experiment. To illustrate them, we show in Figs. 9 and 10 the found $L = 4$ chiral states with different geometry of the phase domain walls. In Fig. 9 domain wall connects adjacent sides of the sample, whereas in 10 it spans across the sample. Such configurations of the domain walls strongly affect the observed vortex states, since the vortex configuration is now formed in a three-fold competition between the sample geometry, number of vortices, and the geometry of the phase domain wall.

The presence of domain walls and favorable vortex splitting can therefore result in a very pronounced symmetry breaking, as shown in Fig. 11 for the $L = 1$ state. Due to the domain wall running across the sample, the vortices in different bands separate along that line, and the vortex present in the first condensate is not in the middle of the sample, which is directly observable in e.g. scanning probe experiments. This configuration notably breaks the fourfold symmetry. By flipping the sign of the phase difference in both domains in Fig. 11, the magnetic signature of the asymmetry will shift to the left instead of to the right.

Finally, we note that although states with domain wall are more rich and intriguing, it is actually the chiral states without domain walls that are the ground states of this system at any given magnetic field. This suggests that latter states will be more likely found in experiments on chiral superconductors, but states with domain walls

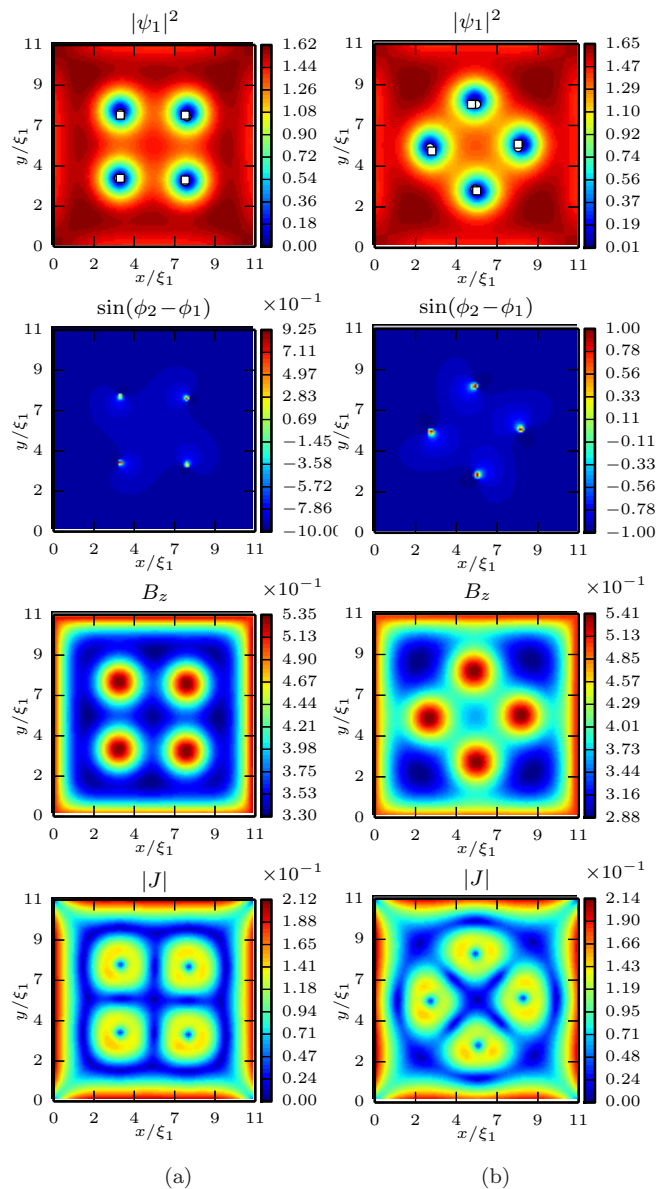


FIG. 5: Two found configurations of four vortices in a chiral vortex state, presented in the same manner as Fig. 3.

remain observable in e.g. field-cooled experiments.

C. Chiral fractional vortex states

In the previous sections we showed that (1) the system has solutions that behave as conventional vortex matter, where the passive bands show the same behavior as the active band, and (2) that there exist chiral solutions that actually have a lower free energy than the conventional vortex states in the frustrated system. Excited chiral states with phase domain walls were also possible. The latter actually stimulates vortex splitting along the domain walls, as discussed in Ref.⁴². We introduced

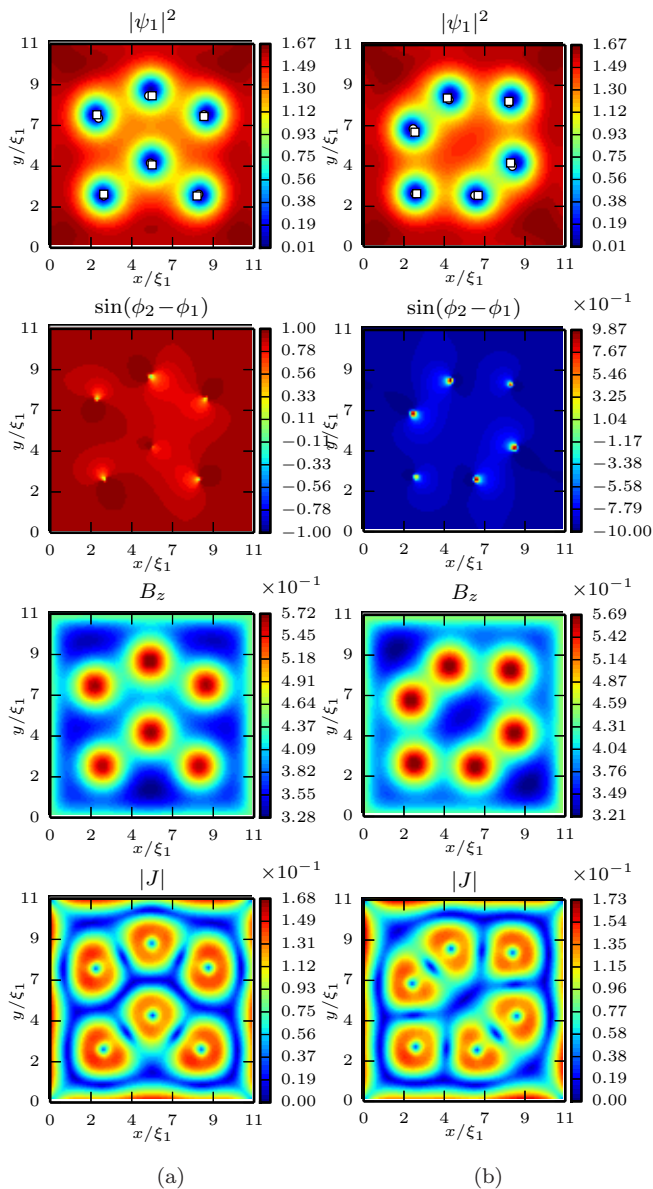


FIG. 6: Two found configurations of six vortices in a chiral vortex state, presented in the same manner as Fig. 5.

a term ‘split-core vortex’ as a vortex that is non composite, i.e. the position of the vortex core in the three band-condensates is different. On the other hand, the difference in length-scales between the condensates¹² should further affect the frustration, and according to Refs.^{30,35} it could also lead to fractional vorticity, where different number of vortices is found in different bands. The interplay of latter effects can therefore create numerous new equilibria in the system, which we will classify by the number of vortices in the passive bands compared to the active band for our choice of parameters. It should be noted however, that the usual fractional states in mesoscopic multiband superconductors, due to only competition of length scales (as discussed in Refs.^{30,35}), are not

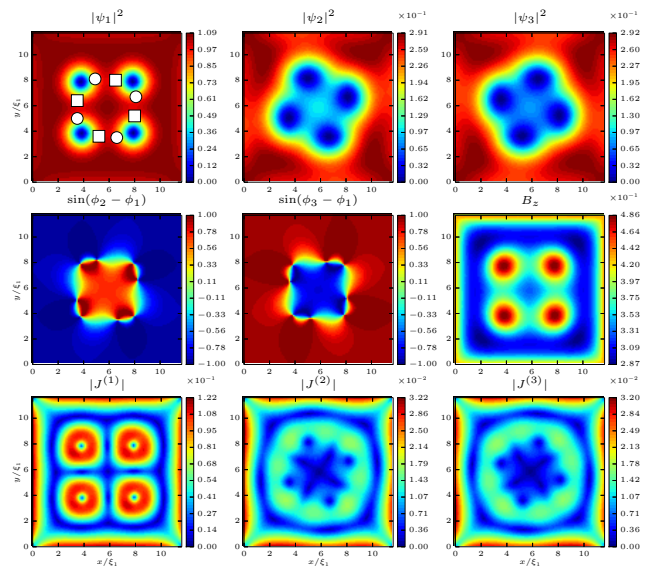


FIG. 7: Chiral $L = 4$ vortex state with an internal phase domain wall, illustrated in the same format as Fig. 1.

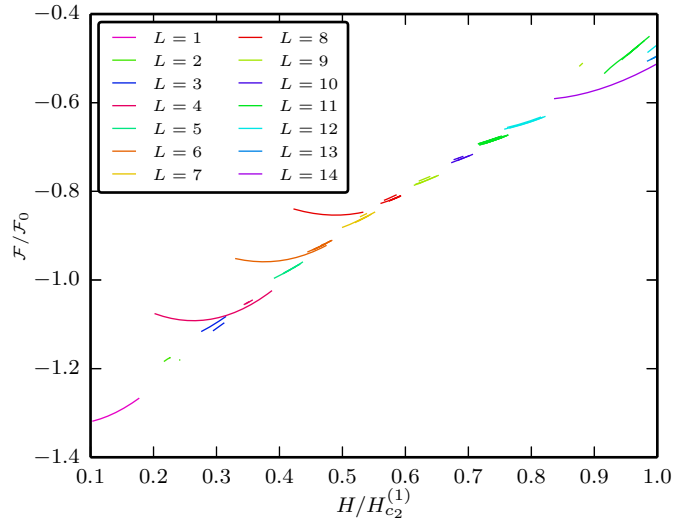


FIG. 8: Energy curves of the found chiral vortex states with phase domain walls, and consequently split-core vortices.

present in our system. In the absence of phase frustration, we have only found composite vortices for the chosen microscopic parameters (see Fig. 2). Therefore, the fractional vortices in the following sections are induced solely by phase frustration and time-reversal symmetry breaking, and are therefore called ‘chiral fractional vortices’.

1. Larger vorticity in passive condensates

We found a multitude of fractional states with more vortices in the passive bands compared to the active band. In Fig. 12 we show the energy spectrum of found

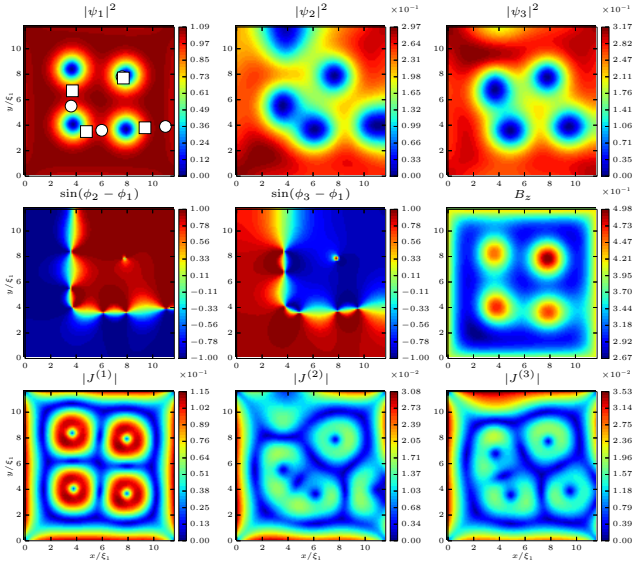


FIG. 9: Chiral $L = 4$ vortex state with phase domain wall connecting adjacent sides of the sample, illustrated in the same format as Fig. 7 for facilitated comparison of all relevant quantities.

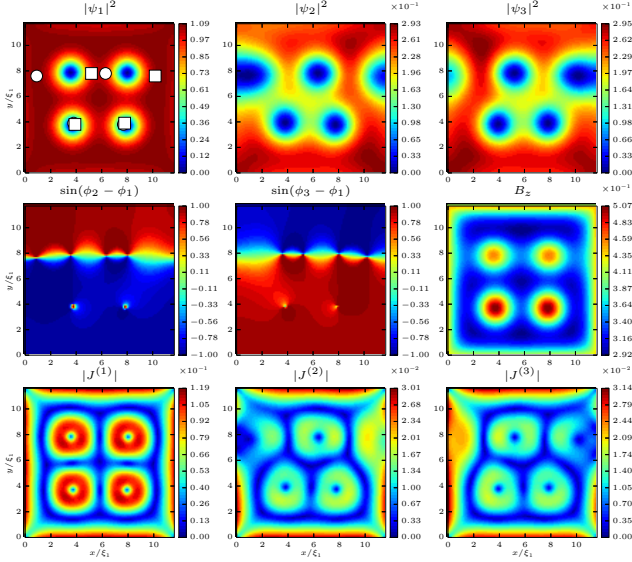


FIG. 10: *Idem.* as Fig. 9, but for a state with phase domain spanning across the sample.

states without a phase domain wall, and one additional fractional vortex in the passive bands. The observed behavior is fairly conventional, with exception of the less parabolic shape of the energy curves due to the fact that fractional vortices are easily expelled in lowered magnetic field.

In Fig. 13 we show one example of a chiral fractional state from Fig. 12. We find that fractional vortices avoid each other due to time-reversal symmetry breaking, and in this particular example one vortex can be found in passive bands, whereas none is present in the active band.

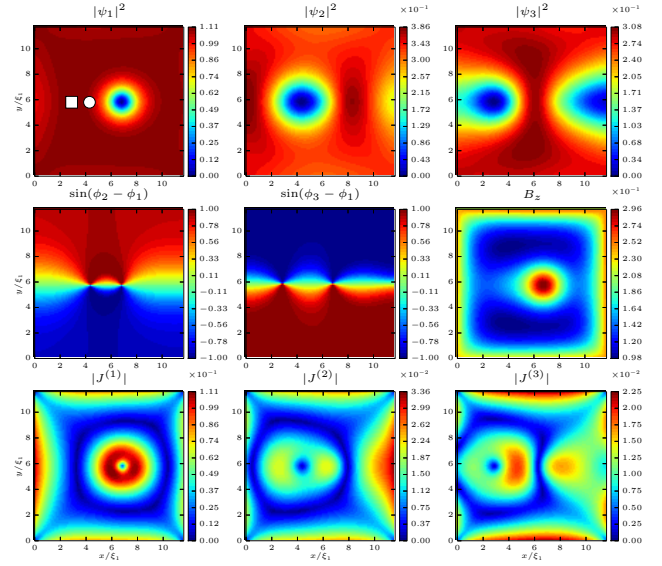


FIG. 11: Chiral vortex state for $L = 1$ with notably broken spatial symmetry.

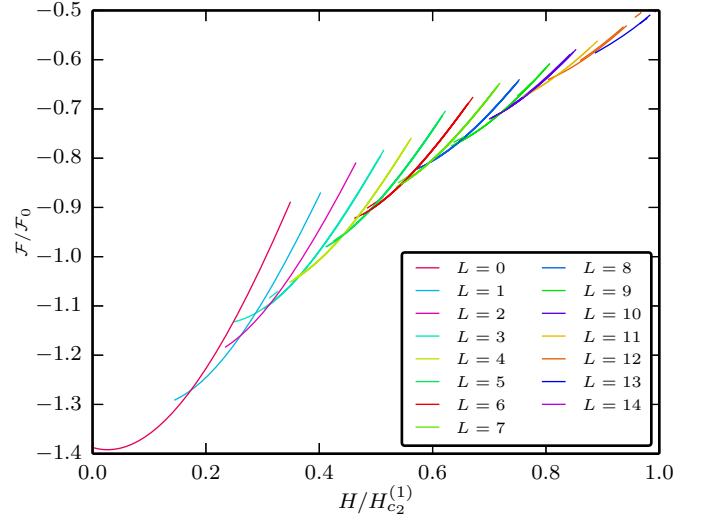


FIG. 12: Energy curves of the chiral fractional states with one fractional vortex in the passive bands $(L_1, L_2, L_3) = (L, L + 1, L + 1)$, without domains in the phase difference between the band-condensates.

We label such state as $(L_1, L_2, L_3) = (0, 1, 1)$. This state exhibits non-integer flux, spatial asymmetry of the condensates, and stray magnetic field whose profile does not directly show presence of any vortices. The difference in vorticity between the bands can actually be larger than 1. In other words, it is possible to have more than one chiral fractional vortex in the system. In our simulations we found states with up to six (!) extra vortices in each passive band compared to the active one, an example of which is shown in Fig. 14 for the state $(9, 15, 15)$.

Finally, in Fig. 15 we relax the condition on the phase, allow for the formation of the phase domain walls, and

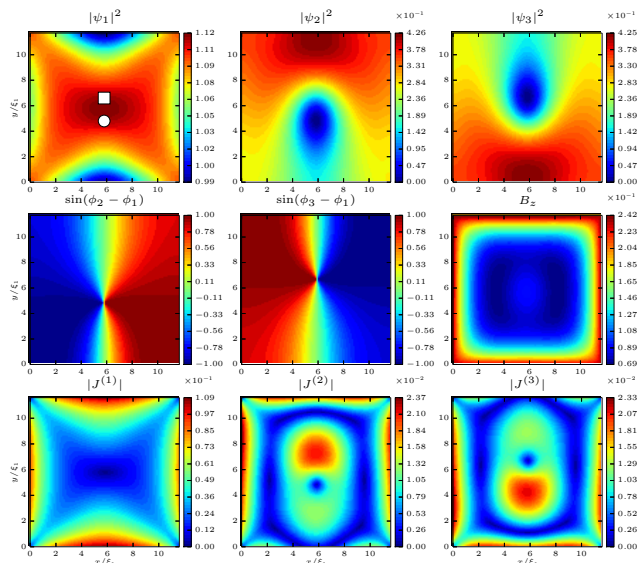


FIG. 13: The chiral fractional vortex state $(0, 1, 1)$.

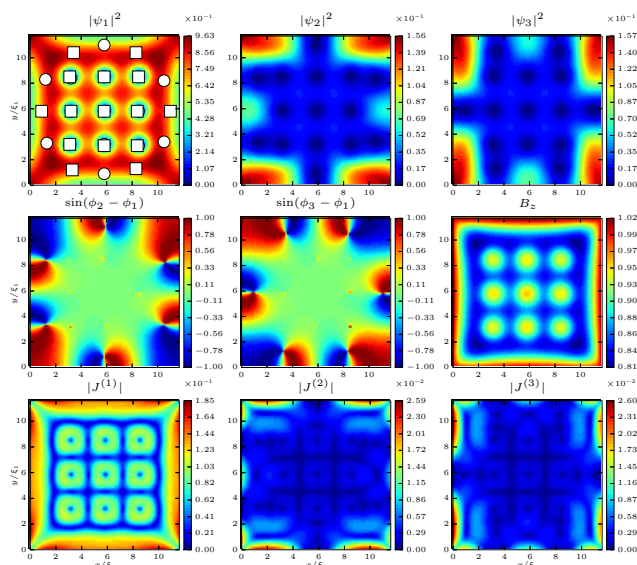


FIG. 14: The chiral fractional vortex state $(9, 15, 15)$, showing the case of 6 fractional vortices aside 9 composite ones in the same sample.

show the energy of all found states with four chiral fractional vortices, i.e. all possible states $(L, L+4, L+4)$. We see that some vorticities have two or more equilibria with a slightly different energy. We show an example of this meta-stability, found for the state $(4, 8, 8)$, in Fig. 16. As was the case for the chiral vortex states with phase domain walls, the states with internal domain wall always have higher energy compared to the state without the domain wall, but show more pronounced fractionalisation, i.e. more separated vortex cores in the band condensates.

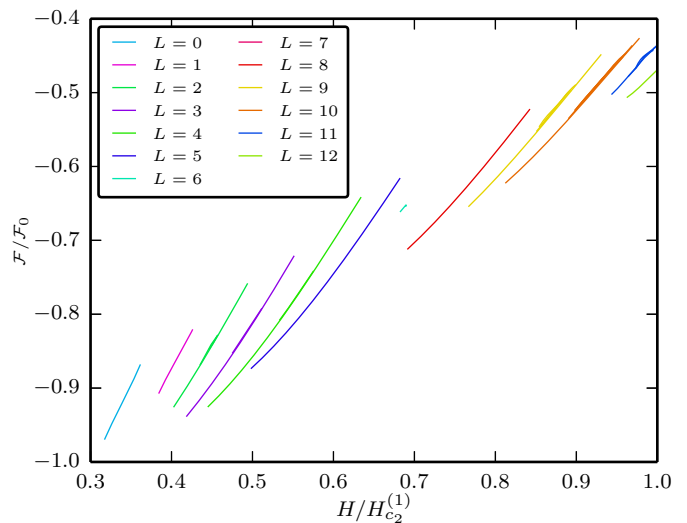


FIG. 15: Energy of all found vortex states with four chiral fractional vortices in the passive bands, $(L, L+4, L+4)$, regardless of the phase distribution.

2. Lower vorticity in passive condensates

It is also possible that the passive condensates have less vortices than the active condensate, even though such states for our parameters have narrower range of stability than those with more vortices in the passive bands considered in previous subsection. Fig. 17 shows the energy as a function of the applied field for all the $(L+n, L, L)$ states, having $n=1, 2$ fewer vortices in the passive condensates. We note that for the chosen set of parameters there are only states found for either one or two extra vortices in the active band, indicating that fractional states with more vortices in the active band than in passive bands are indeed less favorable than opposite, which is of course implied by the strong superconductivity in the active band.

In Fig. 18 we show an example of the $(4, 3, 3)$ state with one extra vortex in the active condensate compared to the passive condensates ($n=1$). The frustration is still visible in the loci of the vortex cores, although the fractional vortex is now only present in the active band. However, contrary to other examples of chiral fractional vortices (e.g. in Fig. 16) which were located in the passive bands, the fractional vortex in the active band leaves a clear magnetic signature in the spatial distribution of the magnetic field compared to the three composite vortices, observable by magnetic scanning microscopies (MFM, SHPM, etc.). It is peculiar that in this example we found a phase domain wall running exactly through the fractional vortex, which makes one wonder if other possibilities for the geometry of the domain wall are stable. In Fig. 19 we show one such possibility for the $(4, 3, 3)$ state, exactly opposite to the case of Fig. 18. Now only one vortex is composite, and domain wall runs through remaining three vortices of the first band, and

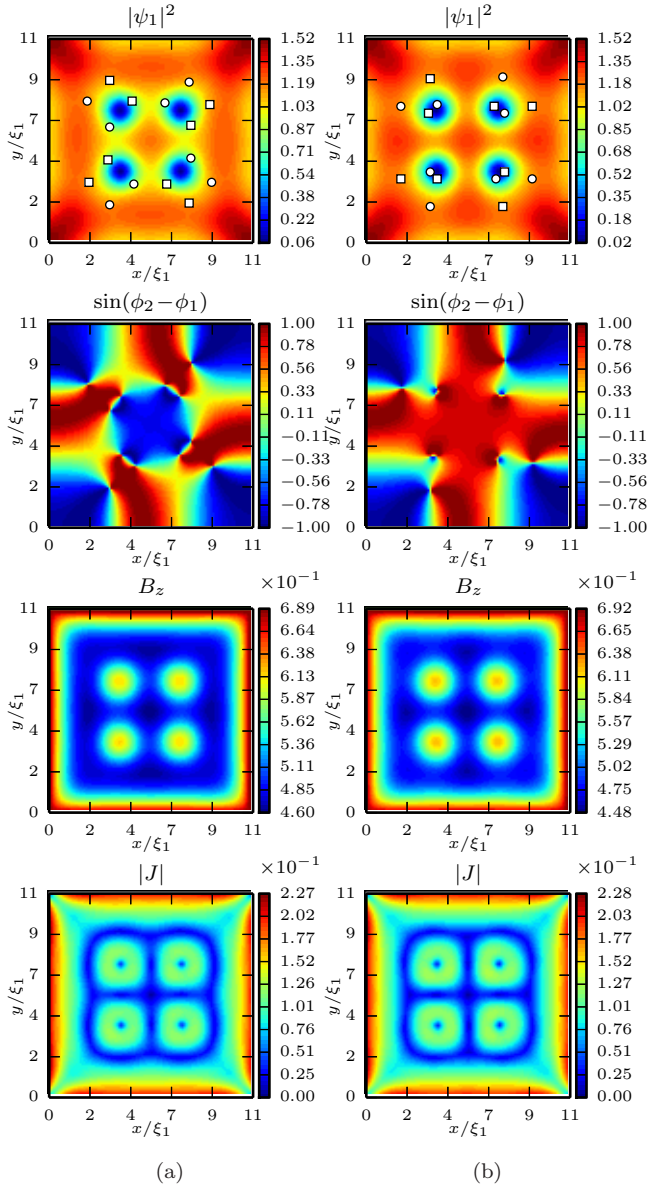


FIG. 16: Vortex state $(4, 8, 8)$, with four split-core vortices in all bands, and four chiral fractional vortices in the second and third bands. (a) A higher energy state, with an internal domain wall; (b) the state with no internal domain wall.

two in each other band, so that we seemingly have one composite and three fractional vortices in the magnetic response of the sample. In fact, there is only one truly fractional vortex on the domain wall, and other two are split-core vortices.

3. Different vorticity in passive condensates

The remaining class of chiral fractional states comprises ones where the number of vortices differs even between the two passive condensates. Fig. 20 shows the

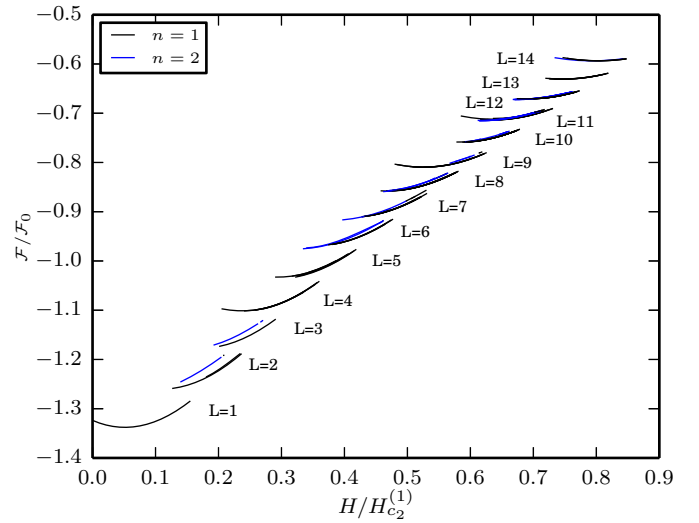


FIG. 17: Energy of all found states with $n = 1, 2$ fewer vortices than in the active condensate, i.e. $(L + n, L, L)$ states, thus comprising n fractional vortices only in the active band.

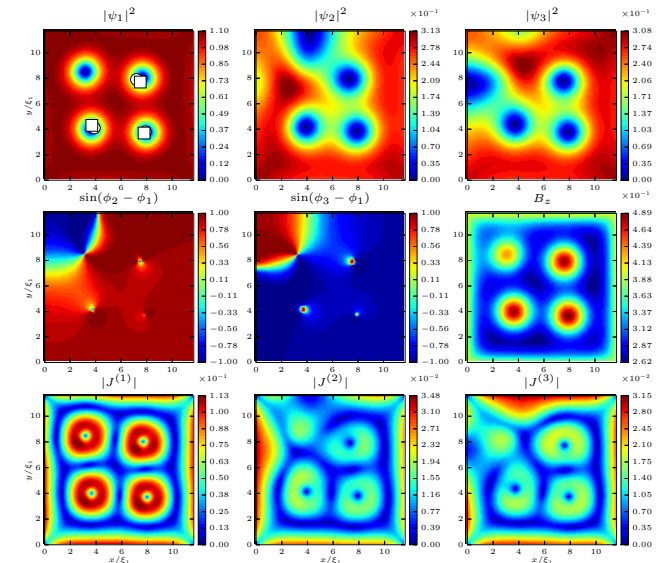


FIG. 18: Example of a chiral state with four vortices in active band, and three vortices in the passive bands. A phase domain wall runs through the single fractional vortex in the first band.

energy dependence on the externally applied magnetic field of all fractional states with different vorticity in the passive condensates. An example of such state is shown in Fig. 21, for the $(2, 3, 2)$ case, i.e. vorticity two in the first and third condensate, but vorticity three in the second. These states are essentially formed in the transition between the states discussed in the previous sections, where one chiral fractional vortex would leave the system before the accompanying fractions vanish as well, and are therefore much less stable than states shown in the pre-

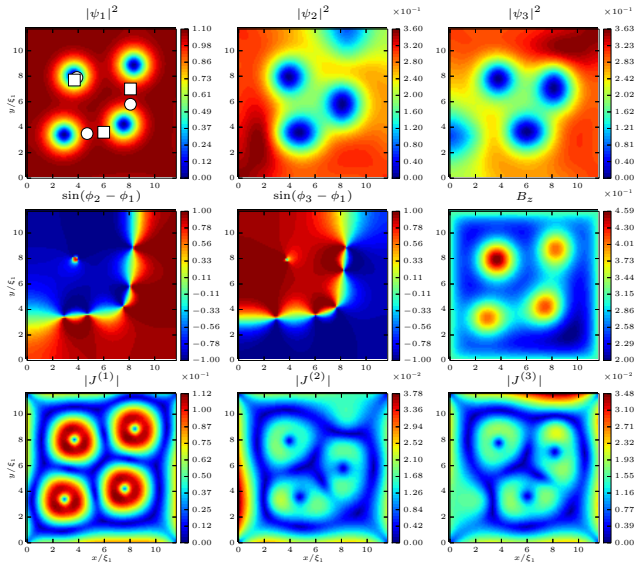


FIG. 19: Another example of a state with same vorticity as in Fig. 18. This state has higher energy than the state shown in Fig. 18 due to the different symmetry and arrangement of vortices along the domain wall.

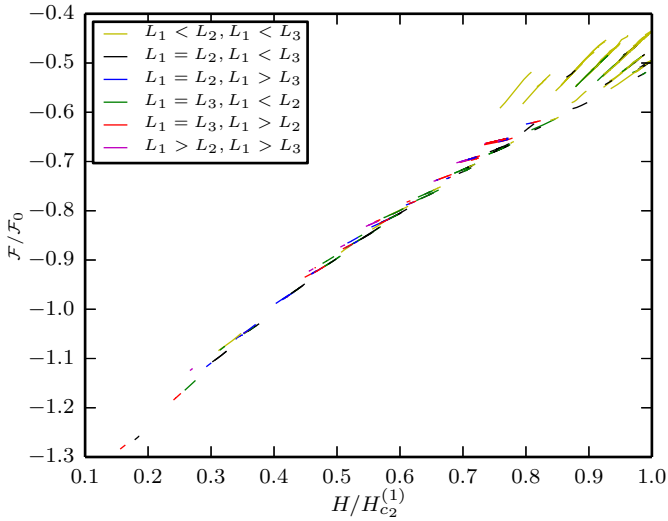


FIG. 20: Energy of all found vortex states where the number of vortices in the second and third condensates are different.

vious sections. The exception are the states with larger vorticities in the passive bands, at higher applied fields; they are seemingly more stable, but that is of pure academic value since at such high fields and vorticities the passive bands are extremely depleted. It is worth noting here that the rarity of such states should be expected since the parameters of the passive bands are taken identical. Should one investigate systems where all the bands have significantly different parameters, one would expect these states to become more common.

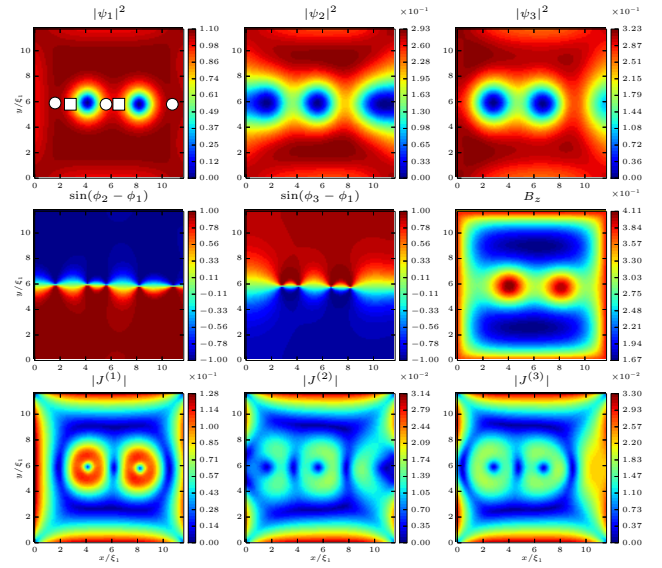


FIG. 21: Vortex state with three vortices in the second condensate and two in the first and third condensate, with an internal phase domain wall and clear symmetry breaking.

IV. CONCLUSION

In summary, we have studied in detail the mixed state of a mesoscopic three-band superconductor with a frustrated choice of Josephson couplings between the band-condensates, using the three-component Ginzburg-Landau theory. We examined, described, and classified all the found vortex states in a mesoscopic three-band system (please see the interactive visualization tool of all states in the Supplementary Material), some of which can be called *conventional* - with composite vortex cores in different bands (i.e. their cores are coaxial in three condensates), and no phase difference between the band-condensates. As a first important result, we showed that the ground state of the system are the *chiral* states, in which phase difference is found between the band condensates, but vortices are still composite. This is the first such example of the chiral state as the ground state of the system at all magnetic fields. On the other hand, a state with non-composite (called ‘split-core’) vortices was predicted as an excited state in Ref.⁴² but for an existing internal phase domain wall on which vortices are located. Indeed, we have also found such *chiral split-core* vortex states in the mesoscopic system, where the presence of domain walls not only introduces split-core vortices, but can also lead to symmetry breaking, in more ways than one since the domain wall can have different configurations with respect to sample boundaries. Finally, in a mesoscopic system, the different effect of confinement on different condensates can stabilize states with fractional flux, i.e. different vorticity in different bands, as is well known from the earlier two-band studies^{30,35}. In the chiral case, vortex fractions in different bands avoid each other, and can differ in numbers, which opens the *chiral*

fractional class of states. Here fractionalisation follows from the domain walls of the phase difference between bands interacting with the sample boundaries and favoring vortex splitting, not from different length scales of the condensates. This plethora of distinct classes of vortex states makes a three-band mesoscopic system an excellent playground for further theoretical and experimental studies, where dynamics of condensates, vortices, and phase slippage⁵¹ must be correspondingly rich, especially since many of the recently discovered iron-based superconductors have 3+ overlapping bands.

Acknowledgments

This work was supported by the Flemish Science Foundation (FWO). Critical remarks of Lucia Komendová are gratefully acknowledged.

- ¹ J. Nagamatsu, N. Nakagawa, T. Muranaka, Y. Zenitani, and J. Akimitsu, *Nature* **410**, 63 (2001).
- ² F. Giubileo, D. Roditchev, W. Sacks, R. Lamy, D. Thanh, J. Klein, S. Miraglia, D. Fruchart, J. Marcus, and P. Monod, *Phys. Rev. Lett.* **87**, 177008 (2001).
- ³ M. Iavarone, G. Karapetrov, A. E. Koshelev, W. K. Kwok, G. W. Crabtree, D. G. Hinks, W. N. Kang, E.-M. Choi, H.-J. Kim, and S. I. Lee, *Phys. Rev. Lett.* **89**, 187002 (2002).
- ⁴ P. Szabó, P. Samuely, J. Kačmarčík, T. Klein, J. Marcus, D. Fruchart, S. Miraglia, C. Marcenat, and A. Jansen, *Phys. Rev. Lett.* **87**, 137005 (2001).
- ⁵ H. Schmidt, J. Zasadzinski, K. Gray, and D. Hinks, *Phys. Rev. Lett.* **88**, 127002 (2002).
- ⁶ F. Bouquet, R. Fisher, N. Phillips, D. Hinks, and J. Jorgensen, *Phys. Rev. Lett.* **87**, 047001 (2001).
- ⁷ H. Yang, J.-Y. Lin, H. Li, F. Hsu, C. Liu, S.-C. Li, R.-C. Yu, and C.-Q. Jin, *Phys. Rev. Lett.* **87**, 167003 (2001).
- ⁸ H. Suhl, B. T. Matthias, and L. R. Walker, *Phys. Rev. Lett.* **3**, 552 (1959).
- ⁹ V. A. Moskalenko, *Fiz. Met. Metalloved.* **8**, 503 (1959).
- ¹⁰ E. Babaev and M. Speight, *Phys. Rev. B* **72**, 180502 (2005).
- ¹¹ A. Chaves, L. Komendová, M. V. Milošević, J. S. Andrade, G. A. Farias, and F. M. Peeters, *Phys. Rev. B* **83**, 214523 (2011).
- ¹² L. Komendová, M. V. Milošević, A. A. Shanenko, and F. M. Peeters, *Phys. Rev. B* **84**, 064522 (2011).
- ¹³ A. A. Shanenko, M. V. Milošević, F. M. Peeters, and A. V. Vagov, *Phys. Rev. Lett.* **106**, 047005 (2011).
- ¹⁴ S.-Z. Lin and X. Hu, *Phys. Rev. B* **84**, 214505 (2011).
- ¹⁵ V. Moshchalkov, M. Menghini, T. Nishio, Q. H. Chen, A. V. Silhanek, V. H. Dao, L. F. Chibotaru, N. D. Zhigadlo, and J. Karpinski, *Phys. Rev. Lett.* **102**, 117001 (2009).
- ¹⁶ T. Nishio, V. H. Dao, Q. Chen, L. F. Chibotaru, K. Kadowaki, and V. V. Moshchalkov, *Phys. Rev. B* **81**, 020506 (2010).
- ¹⁷ Y. Tanaka, *Phys. Rev. Lett.* **88**, 017002 (2001).
- ¹⁸ E. Babaev, *Phys. Rev. Lett.* **89**, 067001 (2002).
- ¹⁹ E. Babaev, J. Jäykkä, and M. Speight, *Phys. Rev. Lett.* **103**, 237002 (2009).
- ²⁰ L. Komendová, Y. Chen, A. A. Shanenko, M. V. Milošević, and F. M. Peeters, *Phys. Rev. Lett.* **108**, 207002 (2012).
- ²¹ B. Baelus and F. M. Peeters, *Phys. Rev. B* **65**, 104515 (2002).
- ²² V. Schweigert and F. M. Peeters, *Phys. Rev. B* **60**, 3084 (1999).
- ²³ W. Little and R. Parks, *Phys. Rev. Lett.* **9**, 9 (1962).
- ²⁴ V. Bruyndoncx, L. Van Look, M. Verschuere, and V. Moshchalkov, *Phys. Rev. B* **60**, 10468 (1999).
- ²⁵ A. Kanda, B. J. Baelus, F. M. Peeters, K. Kadowaki, and Y. Ootuka, *Phys. Rev. Lett.* **93**, 257002 (2004).
- ²⁶ M. V. Milošević, A. Kanda, S. Hatsumi, F. M. Peeters, and Y. Ootuka, *Phys. Rev. Lett.* **103**, 217003 (2009).
- ²⁷ B. Xu, M. V. Milošević, S.-H. Lin, F. M. Peeters, and B. Jankó, *Phys. Rev. Lett.* **107**, 057002 (2011).
- ²⁸ D. S. Golubović, M. V. Milošević, F. M. Peeters, and V. V. Moshchalkov, *Phys. Rev. B* **71**, 180502 (2005).
- ²⁹ V. Schweigert, F. M. Peeters, and P. S. Deo, *Phys. Rev. Lett.* **81**, 2783 (1998).
- ³⁰ R. Geurts, M. V. Milošević, and F. M. Peeters, *Phys. Rev. B* **81**, 214514 (2010).
- ³¹ P. J. Pereira, L. F. Chibotaru, and V. Moshchalkov, *Phys. Rev. B* **84**, 144504 (2011).
- ³² M. A. Silaev, *Phys. Rev. B* **83**, 144519 (2011).
- ³³ J. C. Piña, C. C. de Souza Silva, and M. V. Milošević, *Phys. Rev. B* **86**, 024512 (2012).
- ³⁴ A. Col, V. Geshkenbein, and G. Blatter, *Phys. Rev. Lett.* **94**, 097001 (2005).
- ³⁵ L. F. Chibotaru and V. H. Dao, *Phys. Rev. B* **81**, 020502 (2010).
- ³⁶ L. F. Chibotaru, V. H. Dao, and A. Ceulemans, *Europhysics Lett. (EPL)* **78**, 47001 (2007).
- ³⁷ Y. Kamihara, T. Watanabe, M. Hirano, and H. Hosono, *Journal of the American Chemical Society* **130**, 3296 (2008).
- ³⁸ X. H. Chen, T. Wu, G. Wu, R. H. Liu, H. Chen, and D. F. Fang, *Nature* **453**, 761 (2008), 0803.3603.
- ³⁹ G. F. Chen, Z. Li, D. Wu, G. Li, W. Z. Hu, J. Dong, P. Zheng, J. L. Luo, and N. L. Wang, *Phys. Rev. Lett.* **100**, 247002 (2008).
- ⁴⁰ D. Lu, M. Yi, S.-K. Mo, J. Analytis, J.-H. Chu, a.S. Erickson, D. Singh, Z. Hussain, T. Geballe, I. Fisher, *et al.*, *Physica C* **469**, 452 (2009).
- ⁴¹ K. Kuroki, S. Onari, R. Arita, H. Usui, Y. Tanaka, H. Kontani, and H. Aoki, *Phys. Rev. Lett.* **101**, 087004 (2008).
- ⁴² J. Garaud, J. Carlström, and E. Babaev, *Phys. Rev. Lett.* **107**, 197001 (2011).
- ⁴³ J. Garaud, J. Carlström, E. Babaev, and M. Speight, *Phys. Rev. B* **87**, 014507 (2013).
- ⁴⁴ V. Stanev and Z. Tešanović, *Phys. Rev. B* **81**, 134522 (2010).
- ⁴⁵ N. V. Orlova, A. A. Shanenko, M. V. Milošević, F. M. Peeters, A. V. Vagov, and V. M. Axt, *Phys. Rev. B* **87**, 134510 (2013).
- ⁴⁶ S. Benson, L. C. McInnes, J. Moré, T. Munson, and J. Sarich, *TAO User Manual (Revision 1.9)*, Tech. Rep. ANL/MCS-TM-242, Mathematics and Computer Science Division, Argonne National Laboratory (2007), <http://www.mcs.anl.gov/tao>.
- ⁴⁷ S. Balay, K. Buschelman, V. Eijkhout, W. D. Gropp, D. Kaushik, M. G. Knepley, L. C. McInnes, B. F. Smith, and H. Zhang, *PETSc Users Manual*, Tech. Rep. ANL-95/11 - Revision 3.0.0, Argonne National Laboratory (2008).
- ⁴⁸ J. Jäykkä and J. M. Speight, *Phys. Rev. D* **84**, 125035, 125035 (2011).
- ⁴⁹ W. D. Gropp, H. G. Kaper, G. K. Leaf, D. M. Levine, M. Palumbo, and V. M. Vinokur, *J. Comp. Phys.* **123**, 254 (1996).
- ⁵⁰ M. V. Milošević and R. Geurts, *Physica C* **470**, 791 (2010).
- ⁵¹ G. R. Berdiyrov, M. V. Milošević, and F. M. Peeters, *Phys. Rev. B* **79**, 184506 (2009).